Research Square

Preprints are preliminary reports that have not undergone peer review.
They should not be considered conclusive, used to inform clinical practice,
or referenced by the media as validated information.

Thin-film lithium niobate photonic platform for CV-QKD in inter-satellite links: a feasibility study through chip design, characterization, and radiation testing

José C. Guerra Copete

jcguerra@arquimea.com

Arquimea Research Center

Diego A. Moreno Ramos

Consejo Superior de Investigaciones Científicas

Julio E. Posada Román

Arquimea Research Center

Cristina de Dios Fernández

University Carlos III of Madrid

Research Article

Keywords: Quantum communications, QKD, TFLN, Photonics, PIC, Lithium Niobate

Posted Date: November 9th, 2026

DOI: https://doi.org/10.21203/rs.3.rs-11376746/v1

License: This work is licensed under a Creative Commons Attribution 4.0 International License.
Read Full License

Additional Declarations: No competing interests reported.

Thin-film lithium niobate photonic platform for CV-QKD in inter-satellite links: a feasibility study through chip design, characterization, and radiation testing

José C. Guerra Copete[1,2*†], Diego A. Moreno Ramos[1,3†], Julio E. Posada Román[2], Cristina de Dios Fernández[1]

[1]Electronic Technology Dept., University Carlos III of Madrid, Avenida de la Universidad, 30, Leganés, 28911, Madrid, Spain.
[2]Arquimea Research Center, Camino de las Mantecas, s/n, San Cristóbal de la Laguna, 38320, S/C de Tenerife, Spain.
[3]Fundamental Physics Institute, Consejo Superior de Investigaciones Científicas, C. de Serrano, 113, Chamartín, 28006, Madrid, Spain.

*Corresponding author(s). E-mail(s): jcguerra@arquimea.com;
Contributing authors: diego.moreno@iff.csic.es;
jeposada@arquimea.com; cdios@ing.uc3m.es;
†These authors contributed equally to this work.

Abstract

Continuous-variable quantum key distribution (CV-QKD) is a promising route to secure inter-satellite optical links, as it integrates naturally with coherent classical communication technology while offering quantum-based security. However, meeting the stringent size, weight, and power constraints of spaceborne payloads requires a photonic integrated platform that combines high-speed, low-noise modulation with low optical losses. Thin-film lithium niobate (TFLN) is uniquely suited to this role thanks to its outstanding electro-optic properties, but its application to CV-QKD has remained unexplored. In this work, we present a feasibility study of a CV-QKD transceiver architecture on a monolithic TFLN photonic integrated circuit (PIC) oriented towards low Earth orbit inter-satellite links. We design the modulation scheme and QKD architecture on a single TFLN PIC, fabricated through a commercial multi-project wafer run, and experimentally characterize its passive and active building blocks. We further report gamma radiation testing of the fabricated chips up to 47 krad, observing no significant degradation in passive performance, RF response, or IQ modulation fidelity. Building on these experimentally measured device parameters, we develop a simulation environment that maps realistic hardware imperfections onto the achievable secret key rate in both fiber and free-space optical channels, obtaining simulated secure key rates in the Mbit/s range at short link distances. These results provide a first hardware-anchored feasibility assessment of CV-QKD on TFLN and outline the design refinements needed to progress towards operational inter-satellite links.

Keywords: Quantum communications, QKD, TFLN, Photonics, PIC, Lithium Niobate

1 Introduction

During recent decades, photonic integrated circuit (PIC) technologies have undergone tremendous growth and are now crucial in sectors such as global telecommunication networks [1–3], where they dominate fiber links all over the world. However, the impact of PIC technology extends beyond this realm. They are now considered a reliable and efficient technology in free space scenarios, such as satellite communications, a sector experiencing a rebirth thanks to the development of new private and governmental constellations [4]. While radio frequency (RF) links have traditionally dominated this scene, their limited bandwidth and susceptibility to interference have pushed research towards free-space optical communications (FSOC) [5]. FSOC offers higher bandwidth, reduced interference, and narrower beam divergence, enabling efficient inter-satellite and satellite-ground links with high-speed data transfer capabilities. PICs stand out as a promising technological platform to realize FSOC due to their compactness, low size, weight and power (SWaP) requirements, high modulation speeds, and scalability through the semiconductor industry production [1, 2, 6, 7].

However, the capabilities of FSOC links require robust security measures, as the propagation of sensitive data through free space introduces critical security vulnerabilities [5, 8]. Quantum Key Distribution (QKD), a cornerstone of the ongoing

second quantum revolution, leverages fundamental quantum principles to provide information-theoretic security by revealing the presence of eavesdropping attempts. This is a second area where PIC technology can impact FSOC. Several QKD approaches naturally align with PIC technology, promising high-data rates and practical integration [6], [9]. Among QKD methodologies, Continuous-Variable QKD (CV-QKD) stands out as particularly advantageous for satellite applications. This is because it seamlessly integrates with existing coherent classical telecommunication infrastructure. CV-QKD achieves this by encoding information into the quadrature components of coherent optical states, effectively bypassing the "single-photon bottleneck" inherent in discrete-variable (DV) systems [6, 10, 11]. However, implementing CV-QKD in the challenging environment of Low Earth Orbit (LEO) demands hardware that not only performs exceptionally well but also adheres to stringent size, weight, and power constraints. Although there is extensive research on QKD for satellite-to-ground communications, such as the Micius satellite experiments achieving secret-key rates (SKR) up to 0.59 Mbit/s [12], and the Jinan-1 satellite demonstrating SKR of 1.07 Mbit/s over 12,900 km with a payload of just 23 kg [13], inter-satellite QKD is now beginning to be studied [14].

It is precisely at this intersection between the rebirth of FSOC and the breakthroughs in QKD where photonic integrated circuits have emerged as the primary route towards the miniaturization and stability required for spaceborne quantum payloads. Integrated CV-QKD has advanced rapidly in recent years. Following the first chip-based demonstration of the Gaussian-modulated coherent state (GMCS) protocol on silicon-on-insulator (SOI) [6], photonic-electronic receivers have enabled CV-QKD at classical telecom symbol rates of 10 GBaud [15], and fully integrated transmitter-receiver systems have recently reached 16 GBaud with secret key rates of hundreds of Mbit/s over metropolitan fiber distances [16], including discrete-modulated (DM) CV implementations exceeding 1 Gbit/s [9]. Transmitter PICs have also been reported on indium phosphide (InP), demonstrating pulsed GMCS operation at the proof-of-concept level [17].

In parallel, Thin-Film Lithium Niobate (TFLN) has emerged as a platform that combines the high electro-optic (EO) efficiency of bulk lithium niobate with the tight optical confinement of nanophotonics [7, 18]. TFLN provides an outstanding EO coefficient ($r_{33} \approx 31$ pm/V), enabling modulators with bandwidths exceeding 100 GHz and ultra-low propagation losses (< 0.1 dB/cm), properties uniquely suited to the high-speed, low-noise modulation required in GMCS protocols [10]. TFLN-based QKD has so far been demonstrated in the discrete-variable domain, including a fully integrated chip-to-chip time-bin system operating at 2.5 GHz [19], monolithic BB84 circuits validated over field-deployed fiber [20], and, very recently, gigahertz-rate integrated receivers for time-bin quantum communication [21]. However, the application of TFLN to *continuous-variable* QKD — and specifically to secure inter-satellite links, where its high modulation efficiency, low drive voltage, and low optical loss directly translate into reduced payload SWaP — remains unexplored.

In this work, we present a feasibility study of a CV-QKD transceiver architecture on a monolithic TFLN PIC targeting low Earth orbit (LEO) inter-satellite links, assessing the security attainable when realistic hardware imperfections are taken into

account. Our contributions are threefold. First, we design a complete high-speed modulation scheme and QKD architecture within a single TFLN PIC, fabricated through a commercial multi-project wafer (MPW) run, and experimentally characterize its passive and active building blocks, including propagation losses, extinction ratios, and half-wave voltages. Second, we report gamma radiation testing of the fabricated TFLN chips up to 47 krad, observing no significant degradation in passive performance, RF response, or IQ modulation fidelity—to our knowledge, the first such validation of active TFLN PICs for space environments. Third, we build a comprehensive simulation environment, anchored to the experimentally measured device parameters, that maps these hardware imperfections onto the secret key rate through a GMCS security analysis, under progressively more realistic conditions in both fiber and free-space optical channels. Our results show that optimized TFLN architectures can achieve simulated SKR in the Mbit/s range at short link distances, establishing a hardware-anchored benchmark and outlining the design refinements—most notably a reduction of the modulator half-wave voltage—needed to progress towards realistic inter-satellite link budgets.

2 Results and Discussion

2.1 TFLN Platform suitability

Choosing a suitable photonic platform is fundamental for realizing reliable integrated quantum communication systems. Since each PIC material platform provides a distinct set of features, it is necessary to assess whether the required functionalities for the PIC are available, while also considering the associated technological requirements. The properties of TFLN are summarized in Table 1 and contrasted with the main technologies currently available.

Table 1 Material platform properties.

Features	**Si**	**InP**	**$LiNbO_3$**	**Si_3N_4**	**GaAs**
Transparency window [μm]	1.2 - 8.5	1.0 - 10.0	0.35 - 5.0	0.4 - 6.5	1.0 - 16.0
$n(\lambda = 1.55\mu m)$, Δn	3.48, 2.04	3.18, 0.20	2.20, 0.76	2.00, 0.56	3.35, 0.35
Optical gain (band-gap) [nm]	x	515 - 1550	x	x	1300 - 1600
TO coefficient ($\frac{dn}{dT}$) [K^{-1}]	$1.8 \cdot 10^{-4}$	$2.7 \cdot 10^{-4}$	$3.8 \cdot 10^{-5}$	$2.5 \cdot 10^{-5}$	$2.3 \cdot 10^{-4}$
EO coefficient [pm/V]	x	x	(r_{33}) 31	x	(r_{41}) 1.4
CMOS compatible	Yes	No	No	Yes	No

Silicon-on-insulator (SOI) offers strong optical confinement, CMOS compatibility, and industrial maturity but lacks direct optical gain and an intrinsic EO effect [2], [1]. Indium phosphide (InP) supports active integration via its direct bandgap, yet provides only moderate confinement and limited EO performance [3]. Thin-film lithium niobate (TFLN) combines a large EO coefficient, good confinement, and a broad transparency window extending to sub-micrometer wavelengths, making it ideal for high-speed modulation [7]. Silicon nitride (Si_3N_4) is CMOS-compatible with broadband, low-loss guiding but has no intrinsic gain or EO response [2]. Gallium arsenide

(GaAs) enables active integration and moderate EO effects with wide transparency, but is less mature and not CMOS-compatible [22]. Overall, TFLN emerges as the most suitable platform for the high-speed, low-noise modulation requirements of our application. TFLN's key strength is its high EO coefficient, enabling efficient, $> 100\,\mathrm{GHz}$ modulation bandwidth with CMOS-level drive voltages ($\sim$1.4 V). Realizing and characterizing such bandwidths, however, demands careful management of microwave losses and impedance matching. The half-wave voltage–length product ($V_\pi \cdot L$) typically lies between 1.8 and 5.4 V·cm at telecom wavelengths, yielding modulator lengths from a few millimeters to several centimeters, depending on design trade-offs [7]. TFLN modulators also achieve low insertion loss ($\sim$0.5 dB) and high extinction ratios (20–30 dB, exceeding 40 dB in state-of-the-art devices). Combined with the strong optical confinement of the platform, these features make TFLN a highly attractive choice for high-performance PICs and advanced QKD applications.

2.2 CV-QKD protocol and modulation scheme

Quantum key distribution (QKD) is a cryptographic approach that exploits fundamental principles of quantum mechanics, such as the uncertainty principle and the no-cloning theorem, to enable secure communication between two parties [8]. Unlike classical cryptography, QKD leverages quantum properties to detect the presence of eavesdropping attempts, providing information-theoretic security guarantees.

Continuous-variable (CV) QKD protocols, which encode information onto continuous quantum variables such as the quadrature components of a coherent or squeezed optical state, have gained significant attention due to their compatibility with classical optical communication technologies [6]. Its use of coherent detection, which circumvents the single-photon bottleneck of DV systems, allows for higher transmission rates. Nevertheless, their sensitivity to noise and channel losses makes it challenging for long-distance links, and its security proofs are less well-established than those of DV-QKD [8], [10].

Finally, QKD protocols can work with different types of optical sources [8]. Among these, coherent states are more robust and reliable, which makes them ideal candidates for FSOC links, which are the focus of this work [10].

2.2.1 Protocol description

In figure 1, we can follow the steps of the protocol. In the transceiver side, a strong pilot tone multiplexed with the quantum signal provides precise frequency and phase synchronization between Alice's transmitter and Bob's locally generated LO, essential for correct coherent detection. The optical carrier, operating at 1550 nm, is modulated into discrete pulses at a repetition rate of 250 MHz using a Mach-Zehnder pulse carver. This pulsed configuration facilitates secure discrete-time encoding and synchronization. The quantum information is encoded onto these pulses via QPSK modulation at 250 Mbaud. Simultaneously, the pilot tone undergoes single-sideband modulation with carrier suppression (SSB-CS) at an offset frequency of 1 GHz. The quantum signal is deliberately attenuated to secure photon number levels necessary to leverage the

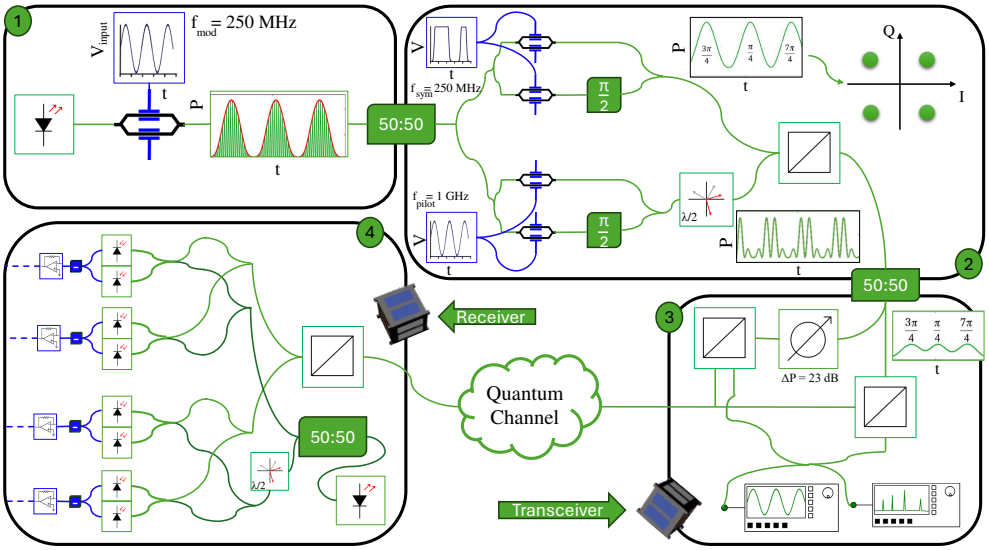


Fig. 1 Scheme of our GMCS-QKD protocol. Step 1: a CW laser signal is carved into discrete pulses, forming the basis of both quantum and reference signals. Step 2: the quantum signal is modulated using QPSK, while a strong pilot tone provides a phase and frequency reference, two IQ modulators are needed for this. Step 3: the quantum signal is then attenuated 23 dB relative to the pilot to ensure security. Next, both signals are propagated through a quantum channel (optical fiber or free space), which introduces loss and potential noise into the transmitted states. Step 4: At the receiver, a local oscillator is used for coherent detection. The incoming signals are mixed with the local oscillator through polarization-diversity and intradyne detection (simultaneous measurement of I and Q).

security advantages of coherent states, approximately in the order of 0.1 to 10 photons per symbol. The operating point of the results reported in this work is specified in Section 2.2.3.

At the receiver, intradyne detection is implemented using a polarization-diversity 90° hybrid, mixing the incoming quantum and pilot signals with the locally generated LO. The quantum signal is measured using low-noise balanced photodetectors optimized for low power levels, while the pilot tone is captured with higher-bandwidth balanced detectors tailored for accurate synchronization. Intradyne detection offers enhanced stability against the frequency and phase drifts common in long-range optical fiber and dynamic satellite environments, and avoids practical vulnerabilities demonstrated against heterodyne receiver implementations [23, 24].

2.2.2 GMCS CV-QKD security analysis

In the Gaussian-Modulated Coherent States (GMCS) CV-QKD protocol, Alice prepares coherent states modulated according to Gaussian distributions and sends them to Bob, who performs the detection. Security in QKD is assessed by comparing the mutual information between Alice and Bob and the information potentially available to an eavesdropper, characterized by the Holevo bound.

These parameters are often derived under asymptotic assumptions (infinitely large number of exchanged symbols), which simplifies the theoretical treatment. While practical systems inherently operate with finite data block sizes, working in this regime provides useful upper bounds on achievable security performance and guides implementations by establishing fundamental limits. The full version of the derivation followed here can be consulted in [10].

The asymptotic security against collective attacks is given by the Devetak-Winter formula. Taking into account realistic aspects of a practical CV-QKD implementation, such as non-ideal reconciliation (reconciliation efficiency β), frame error rates (FER), and the fraction of symbols disclosed for parameter estimation (ν), the secret key fraction is

$$r_{\text{asympt}}^{\text{coll}} \geq (1 - \text{FER})(1 - \nu)\left(\beta I_{AB} - \chi\right), \tag{1}$$

where $r_{\text{asympt}}^{\text{coll}}$ is the asymptotic secret key fraction, I_{AB} is the mutual information between Alice and Bob, and χ is Eve's maximum attainable information (Holevo information).

Two key quantities are therefore required. First, for heterodyne detection, the mutual information can be expressed in terms of the signal-to-noise ratio (SNR) as [10]:

$$I_{AB} = \log_2(1 + \text{SNR}) = \log_2\left(1 + \frac{TV_{\text{mod}}}{2 + \xi}\right), \tag{2}$$

where T is the channel transmittance, V_{mod} the modulation variance, and ξ is the total excess noise at the measurement point.

Second, the Holevo information $\chi(E:B)$ is computed from von Neumann entropies. For an entangling cloner attack (entanglement-based frame), the relevant symplectic eigenvalues needed to recover this quantity can be obtained from

$$a_{EB} = V_{\text{mod}} + 1, \tag{3}$$

$$b_{EB} = TV_{\text{mod}} + \xi + 1, \tag{4}$$

$$c_{EB} = \sqrt{T(V_{\text{mod}}^2 + 2V_{\text{mod}})}. \tag{5}$$

Finally, to perform these calculations we will need to connect measured voltages to shot-noise units (SNU). To achieve this, the measurement setup is calibrated through the mapping factor ϕ

$$\phi \approx P_{LO}\,\rho^2 g^2 B h f, \tag{6}$$

where P_{LO} is the local-oscillator power, ρ is the PIN diode responsivity (A/W), g is the total amplification of the receiver (V/A), B is the electronic bandwidth (Hz), h is Planck's constant, and f the optical frequency. This mapping is experimentally obtained by disconnecting the quantum signal input and measuring the quadratures of a vacuum state.

2.2.3 High-speed modulation scheme

Based on practical implementation constraints and the choice of protocol, we selected Quadrature Phase Shift Keying (QPSK) as the modulation format for our GMCS

CV-QKD scheme. QPSK provides a robust and secure finite-alphabet; its symmetric constellation enhances reconciliation efficiency and aligns seamlessly with readily available hardware and high-speed modulation techniques.

In GMCS CV-QKD, Alice ideally prepares coherent states of the form $|\alpha\rangle = |X + iP\rangle$, where $X, P \sim \mathcal{N}(0, V_{\text{mod}})$. This yields a continuous Gaussian distribution of states in phase space. However, realizing a perfect Gaussian modulation experimentally is challenging. Therefore, QPSK modulation, using four coherent states symmetrically positioned in phase space, approximates the ideal scenario effectively:

$$\alpha_k = \sqrt{n} e^{i\theta_k}, \quad \theta_k \in \left\{ \frac{\pi}{4}, \frac{3\pi}{4}, \frac{5\pi}{4}, \frac{7\pi}{4} \right\}. \tag{7}$$

where n denotes the mean photon number per symbol. It should be noted that employing a QPSK constellation while evaluating security through the Gaussian (GMCS) framework of Section 2.2.2 constitutes an approximation. Rigorous security analyses for discrete-modulated (DM) CV-QKD have been developed in recent years, initially for four-state protocols [25] and later generalized through semidefinite-programming techniques [26, 27], culminating in explicit asymptotic key rate expressions for arbitrary modulation formats [28] and protocol optimizations including postselection [29]. These analyses show that the four-state protocol yields lower secret key rates than its Gaussian counterpart under identical channel conditions, although constellations with as few as a dozen suitably arranged states can closely approach Gaussian performance [16]. In this work, we deliberately adopt the Gaussian security framework of [10] for two reasons. First, the protocol operates in a low modulation variance regime at the channel input: the transmitter terminal losses (more details in Section 2.3) act as trusted attenuation on Alice's side, so that the quantum states entering the untrusted channel carry a mean photon number of $\bar{n} \approx 0.5$ per symbol ($V_{\text{mod}} \approx 1$ SNU at the channel input). At this variance, the QPSK ensemble closely approximates its Gaussian counterpart (the ensemble correlation Z lies within 5% of the Gaussian value), placing the protocol in the regime where discrete-modulation analyses are known to approach Gaussian performance [26, 28]. Second, our primary objective is to isolate and quantify the impact of the photonic hardware (modulator drive voltages, laser noise, detection noise) on achievable security, for which the well-established Gaussian formalism provides a common reference against the integrated CV-QKD literature [6, 15, 17]. The resulting key rates should nonetheless be read as a Gaussian-equivalent hardware benchmark: a dedicated DM analysis at the same operating point would certify strictly lower rates, and constitutes a natural continuation of this work.

2.3 PIC experimental results

The design and fabrication of a photonic integrated circuit (PIC) is a widely diversified process that requires special attention to each step. The first one has already been detailed in section 2.1, assessing the capabilities of the TFLN platform for secure FSO links. Now, we are going to focus on the design and initial characterization stages.

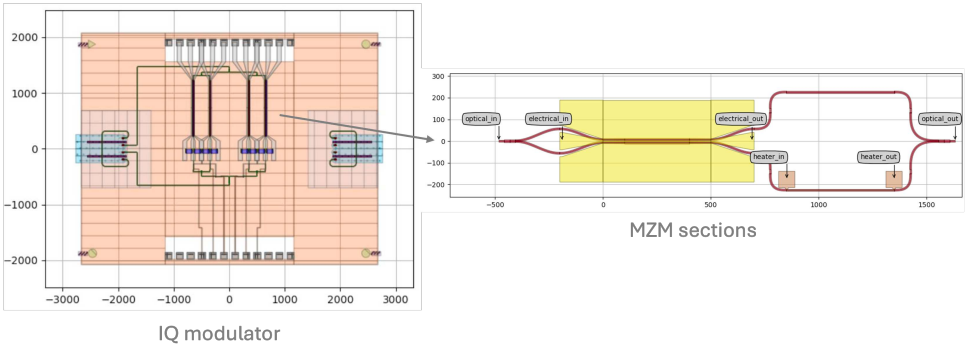


Fig. 2 Left: IQ Modulator used to implement QPSK using two MZMs. Right: Balanced Mach-Zehnder Modulator section (MZM), using both TO and EO phase shifters; the complete layout of the PIC is protected by ARC and cannot be displayed.

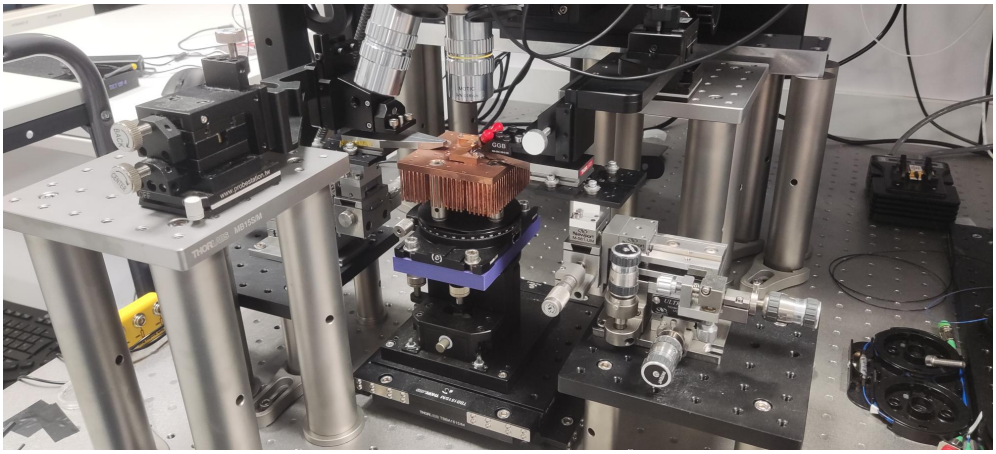


Fig. 3 Experimental setup made of COTS pieces and in-house designed pieces for thermal control.

2.3.1 Design and experimental validation

Regarding the design of the chip, we must distinguish the design of the photonic mask itself and the validation of the used building blocks. The first was performed using Nazca [30], a Python-based open-source tool that allows us to precisely define the architecture and its layout. To include the desired TFLN components, we used a Compact Model Library contained in the Project Design Kit (PDK) developed by the foundry Luxtelligence [31]. In figure 2, we depict the fundamental building blocks as included in the photonic mask sent for fabrication. In the validation of the building blocks we used Luceda IPKISS, the original software used by the foundry to develop the PDK, to study their frequency responses and extract their S-parameters, in the form of matrices, to use them as a first semi-ideal approximation of the PIC's behavior, using libraries including real material data.

Characterization was realized using a custom-built PIC probe station comprising commercial off-the-shelf (COTS) optomechanics from Thorlabs, a microscope head from Motic with an objective for close-up visualization, and discrete lasers from Eblana, controlled via Koheron drivers. Lensed fibers from OZ Optics were used to send the light from the laser to the PIC. Fibers were fixed to the fiber V-grooved holders with Kapton tape. RF signals were sent to the PIC by an arbitrary waveform generator (AWG) via GSG probes, while DC signals were provided by power supplies via wirebonds. Alignment throughout all of the measurements was performed via manual handling of 6-axis nanopositioners at both sides of the chip.

Active media are not available in the commercial MPW stack used here, so edge couplers are required at both facets and the chip cannot operate as a standalone Tx/Rx stage. While rare-earth-doped TFLN gain sections and heterogeneous III-V integration have been demonstrated at research level, they are not yet part of standard foundry offerings, unlike the monolithic active integration available in indium phosphide. This remains the main practical drawback of a monolithic TFLN approach.

For the general assembly, some custom copper pieces were fabricated to set the PIC at the right height, maintaining thermal stability allocating a thermistor and a Peltier thermoelectric element for full thermal control, while not losing range of operation for the fibers at both sides. Custom printed circuit boards (PCBs) were also made to connect the wirebonds to a Samtec receptacle I/O connector for PCBs and have the DC interface outside of the chip, in another custom PCB that allowed an easy handling without compromising the system's mechanical stability (Fig. 3).

The designed PICs included a series of passive test elements to check the behavior and build statistics for this MPW run. Statistics of interest include the distribution of losses per element, the percentage of elements that behave as expected (to validate fabrication processes and fidelity) or the relation between element losses.

All of this data serves as a backbone to validate sources of disturbance. Any source of loss and noise adds up against the system performance, thus tightening the range of several parameters in which we find a positive SKR (a negative SKR would mean no physically secure information). Elements tested are divided among the different paths they follow. Negative losses in the reference waveguide are possible because they are calculated by subtracting the contribution of the simulated insertion losses, index change losses, and measured transmission losses. This means that the theoretical model of light coupling calculated numerically does not correspond well with our physical system.

In general, passive element losses are negligible. 2.5 µm wide waveguides show high losses because, being multimode, they support higher-order modes, giving rise to mode cross-coupling at bends, higher bending losses of non-fundamental modes, and modal noise; short waveguides show very high losses owing to the proximity of the bends along their path. Transmission losses, taken from 1 µm are notable. Crossings have an order of magnitude higher losses than bends, but still around 0.24 dB per crossing are decent levels. Bends have half of the losses with 100 µm of curvature radius than with 50 µm. Transmission losses in standard 1 µm are consistent with expectations, with a total result of $0.336 \pm 0.127\ dB/cm$. Foundry figures of merit report between 0.2 and 0.3 dB/cm for 1 µm waveguides, in reasonable agreement with our measurements.

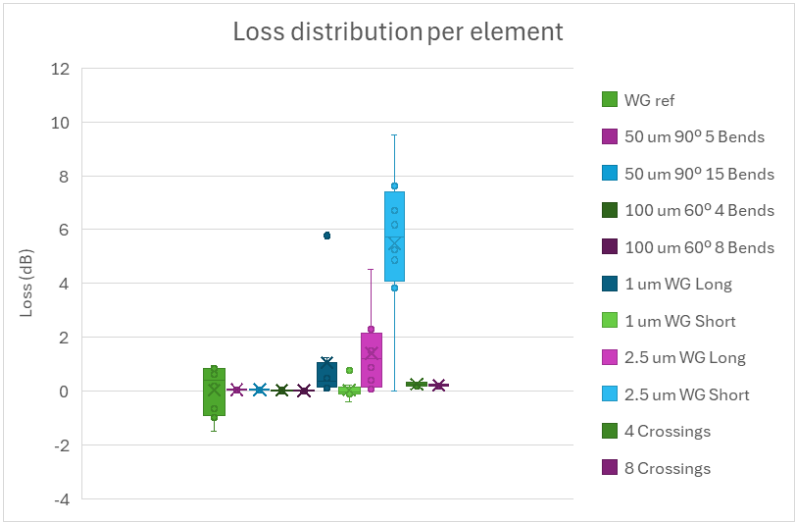


Fig. 4 Passive element losses. Each point denotes a measurement on the named path from a PIC, and the X mark denotes the mean for each path. Box-and-whisker plots represent the extremes and quartiles.

Both figures compare favorably with the propagation losses reported in the PDKs of other material platforms, confirming the strong passive performance of TFLN. In table 2 we show the losses in dB per individual passive element, and in the case of waveguides, per entire path. Eight different PICs were tested entirely, where there was a separate path for each element to be tested.

Path	Mean	Std Dev
Ref waveguide	0.034	0.945
50 µm 90°(5) Bends	0.065	0.024
50 µm 90°(15) Bends	0.056	0.030
100 µm 60°(4) Bends	0.031	0.020
100 µm 60°(8) Bends	0.028	0.017
1 µm WG (Long)	1.219	2.046
1 µm WG (Short)	0.045	0.365
2.5 µm WG (Long)	1.614	1.491
2.5 µm WG (Short)	6.275	1.890
(4) Crossings	0.258	0.061
(8) Crossings	0.223	0.032

Table 2 Summary of losses per element, in dB, on each path

In the selected foundry (Luxtelligence), standard commercial MPW stacks do not allow for DC tuning in RF pads due to fast charge relaxation times ($\ll 1ms$), so DC bias has to be separated using thermo-optical shifters.

Figure 5 shows a DC sweep over a wide voltage range, from which the thermo-optic half-wave voltage is extracted. Independently, the high electro-optic efficiency

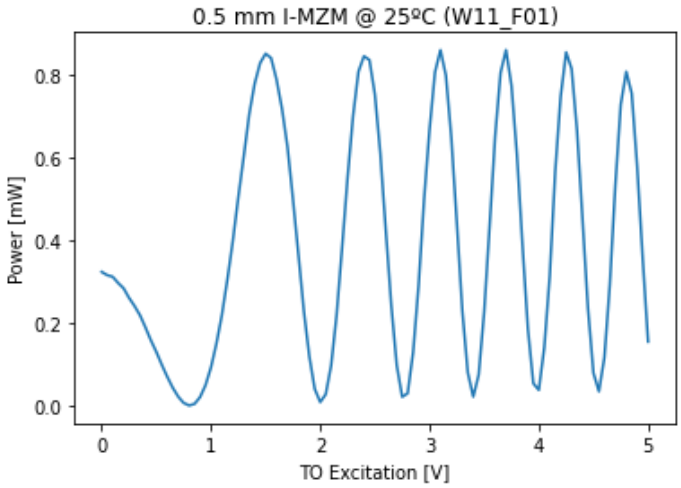


Fig. 5 DC bias sweep of an imbalanced modulator driven by a thermo-optic phase shifter. The optical power follows a sinusoidal dependence on the induced phase shift, which scales with the dissipated electrical power ($\propto V^2$); hence the progressively shorter voltage period at higher bias.

of TFLN leads to a short V_π in the RF sections, enabling shorter modulator lengths or lower drive voltages than in other substrate materials for the same performance. Electro-optical electrodes were fabricated in a push-pull configuration, meaning that for a single signal, the two branches of the MZM are displayed in a GSG configuration and are affected by the same signal, so we need half of the modulating amplitude.

We observed the spectral behavior of the different active elements. This is useful because modulators should show a similar behavior as if we were applying a voltage due to phase imbalance. In general we should see a flat response throughout the whole C-band, indicating that the chip does not get reflections or losses depending on the wavelength, which would affect practical applications. We get a flat response from balanced Mach-Zehnders and other components, and a periodic spectrum on imbalanced MZMs. We studied the effect of the EO pads length and, because of the same imbalance, get a similar spectrum. The difference that length supposed was that for shorter lengths we got a lower extinction ratio.

Modulator length (mm)	0.3	0.5	1.0	2.5
Extinction ratio (dB)	21.77	28.47	28.72	29.66
Free Spectral Range (nm)	4.651	4.698	4.710	4.702

Table 3 Imbalanced modulators characterized on an example chip

2.3.2 Radiation testing

To validate the use of these chips in space environments, we performed total ionizing dose (TID) tests on the fabricated PICs, including their associated electronics. Irradiation was carried out using a Cobalt-60 source placed into a Gammabeam® X200 irradiator. The steady-state irradiation was performed at a dose rate of 230.42 rad(Si)/h, with a relative uncertainty of 4.3% ($k = 2$), up to a total accumulated dose of 47.32 krad(Si), with a dose uniformity over the samples of 93.21%. The test plan complies with the ESCC Basic Specification No. 22900 (Issue 5), "Total Dose Steady-State Irradiation Test Method". Devices were irradiated unbiased, with all electrical contacts left floating, and 8 chips were exposed in 4 pairs to ascending accumulated doses of 10, 20, 36, and 47 krad, with characterization performed after each exposure. For reference, the TID expected over one year in a typical LEO orbit behind 10 mm of aluminum shielding ranges between 4 and 40 krad(Si) [32], so the maximum dose tested exceeds this annual range.

No significant degradation was observed at any dose level. Post-radiation passive measurements were consistent with their pre-radiation counterparts within the repeatability of the setup, RF measurements on different modulators showed no measurable change in half-wave voltage, and IQ modulation tests on the irradiated chips exhibited no measurable degradation of the QPSK constellation.

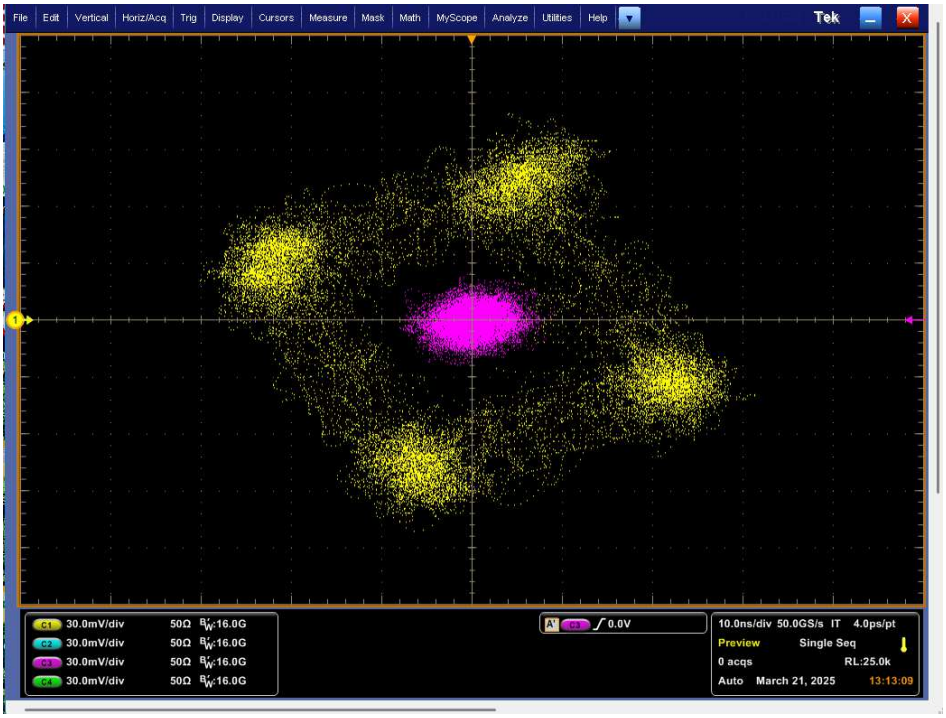


Fig. 6 IQ modulation measured after the highest radiation dose (47 krad). The yellow clusters correspond to the four QPSK symbols; the central magenta trace corresponds to the carrier reserved for the pilot tone.

Figure 6 shows the IQ modulation performance after the highest radiation dose, using the QPSK modulation scheme; the results were similar to those obtained on the PICs before irradiation.

A coherent detector was used to decode the phase of the signal, but we lacked the capabilities to stabilize it. We used one polarization, with polarization maintaining (PM) fibers, while transmitting mainly the TE_0 mode inside the chip. The other one (the magenta signal) is left for a pilot tone as one of the feasible ways to correct the phase in further experiments.

2.4 Signal security simulations

2.4.1 Benchmarking and noise characterization

In this section, we describe the simulation architecture of the experimental setup implemented in Lumerical INTERCONNECT, based on a pilot-assisted coherent intradyne detection scheme suitable for CV-QKD [11]. This experimental setup serves as an effective model for studying inter-satellite quantum communication due to its robust synchronization capabilities and compatibility with high-speed modulation formats. All SKR were calculated using eq. 1 with the parameters $\beta = 0.97$, $FER = 0.05$, and $\nu = 0.25$ taken from [11].

Initially, our objective was to accurately capture realistic operating conditions by incorporating experimentally measured device parameters into our simulation model. Rather than relying exclusively on simulated S-parameters, we introduced passive measurement data obtained directly from the fabricated PIC. Specifically, we incorporated the insertion losses and extinction ratios measured experimentally on a balanced MZM, 5 dB and 20 dB respectively, as well as total losses of the MMI coupler, found to be 3.5 dB, all characterized at our probe station. Additionally, the figure of merit (FOM) ($V_\pi \cdot L$) of the RF-driven MZM sections used for IQ modulation was measured experimentally by Luxtelligence and found to be between 3.0 and 3.5 V·cm. This was also used in our layout, ensuring realistic modeling of the modulator performance.

Before performing detailed parameter sweeps, it was crucial to identify the sources of noise impacting the QKD system's performance. The noise sources modeled in INTERCONNECT included: shot noise, the inherent quantum noise due to the discrete nature of photons, providing the fundamental limit to measurement accuracy; Relative Intensity Noise (RIN), amplitude fluctuations of the laser source affecting signal stability; linewidth, frequency fluctuations causing phase drifts, critical in coherent detection systems. It is essential to highlight the interrelation between RIN and linewidth, as both typically increase with decreased laser power; modulation noise: non-idealities arising from deviations in MZM operating voltages and imperfections in RF drivers; dark current and detection noise, thermal and electronic noise in the photodetectors, quantified through noise-equivalent power (NEP) data; phase recovery noise, residual phase errors following correction using pilot tones; fiber losses and dispersion, optical losses and signal distortion in the transmission medium, initially modeled for optical fiber. This benchmarking phase was carried out at a fixed channel distance of 13 km.

The first significant analysis focused on optimizing the operating parameters of the MZM. First, we performed a diagnostic sweep of the applied RF voltage to visualize its transfer function. Following our first chip prototype, the active RF and DC sections of our TFLN MZM were designed to be 1.0 mm long for the first chip prototype. Based on the experimentally measured FOM, this length corresponds to $V_\pi^{RF} = 35$ V and $V_\pi^{DC} = 0.82$ V respectively.

On the other hand, the input bias voltage determines the modulator's operating point. We observed, as expected, maximum transmission at V = 0. Whereas the quadrature point, which linearizes the modulation response and maximizes sensitivity, occurred at $V = V_{\frac{\pi}{2}} = 17.5$ V. Typically, this quadrature point is chosen by setting the DC bias voltage to $V_{bias} = V_{\frac{\pi}{2}}$ in order to optimize modulation efficiency. However, for the quantum signal part, minimizing excess noise and maximizing security was prioritized over modulation linearity. By setting $V_{bias} = 0$, we achieved the highest possible SNR, though at the expense of suboptimal modulation efficiency. This trade-off affects the clarity of the received symbol constellations at the protocol's output, as we will show later in a more complete analysis.

Given that the initially calculated V_π^{RF} of 35 V was relatively high, potentially increasing modulation-induced noise, we investigated lower values of 17.50, 8.75, and 8.00 V. The optimal balance between mutual information and Holevo bound, which indicate maximal protocol security, was obtained at $V_\pi^{RF} = 8$ V, the lowest tested value. Further reductions in V_π^{RF} were considered; however, with our current $V_\pi \cdot L$ FOM (L = 4.375 mm), lowering this value further would require an RF active length approaching the centimeter scale, compromising the compactness and integrability of the PIC. Such trade-offs are common in PIC design, emphasizing the necessity of balancing performance, efficiency, and chip size constraints to achieve optimal overall system performance.

For the modulation of the pilot signal, the V_π^{RF} was similarly adapted to 8 V. In this context, reducing excess noise was less critical because the pilot signal is inherently stronger, and our priority was achieving optimal modulation efficiency rather than maximizing the SNR. Therefore, we conducted a sweep of the V_{bias} applied to one arm of the pilot signal MZM to identify the best operational point for security, as depicted in figure 7 (a). The highest SKR (0.92 Mbit/s) was observed at a V_{bias} of -1.75 V.

After analyzing modulation noise, we studied the effects of other critical sources of noise, starting with the transmitter laser. Initially, we evaluated the impact of laser power while keeping the linewidth and RIN constant. Conducting parameter sweeps by varying one parameter while keeping the other two constant allowed for isolated assessment of each parameter's impact. While physically, these parameters are often interrelated (for example, linewidth and RIN typically increase as laser power decreases), isolating them provides valuable insight into optimizing each independently before addressing complex combined effects.

As illustrated in figure 7 (b), the highest laser power improved modulation efficiency but also increased the excess noise, since the residual phase error left by the pilot-assisted recovery scales with the modulation variance; the resulting growth in Holevo information outpaced the gain in mutual information, aborting the protocol. Reducing the power again improved security until reaching a point of insufficient SNR

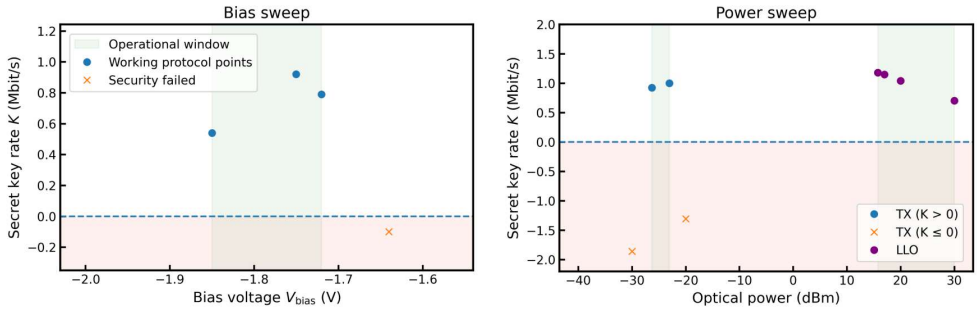


Fig. 7 (a) SKR for different V_{bias} values of the MZMs. (b) SKR for the parameter sweeps of the TX laser and the LLO; marker meanings are given in the legend. RIN has no specific marker since its effect on the SKR is not noticeable at this scale.

to sustain secure communication. The optimal transmitter laser power was found to be -23.01 dBm, with an overall improvement of SKR = 1.1 Mbit/s. Subsequently, independent sweeps were performed for laser linewidth and RIN. For linewidth, typical industry values range between 1 MHz to 10 MHz, although low-power lasers can achieve linewidths as narrow as 50 kHz. Our simulations showed that typical linewidths induced excessive phase errors, severely compromising security. Surprisingly, extremely narrow linewidths also presented borderline security issues, suggesting further investigation into associated RIN impacts at these linewidths is warranted, finding the optimal point at $\Delta\nu = 575kHz$ with more than three times the last security upgrade, SKR = 3.5 Mbit/s. A separate sweep of the RIN from -125 $\frac{dB}{Hz}$ to -163 $\frac{dB}{Hz}$ showed minimal variations in security parameters, though a modest improvement of 10 kbits/s in the SKR was observed at the lowest values. As coherent detection is, in general, robust to amplitude and phase noise, this is expected from our setup. Ultimately, we selected a RIN of -150 $\frac{dB}{Hz}$.

Once the first laser is settled, the LLO comes into play. Unlike the transmitter laser, the LLO significantly affects the coherent detection process directly and, consequently, the phase recovery accuracy. Due to this critical role, optimal performance was achieved at higher tested power levels, as they provided stronger local oscillator signals, significantly enhancing coherent detection efficiency. Lower LLO power drastically reduced the SNR, increasing the discrepancy between mutual information and the Holevo bound, resulting in a strongly negative key rate, i.e., an aborted protocol with a large gap between the Holevo bound and the mutual information. Regarding the linewidth, the best SKR was obtained for the narrowest tested value (20 kHz), demonstrating the necessity of maintaining high coherence in the local oscillator. However, sweeps of the LLO RIN yielded surprisingly negligible variations in SKR, prompting questions about why these fluctuations in the local oscillator appear less impactful. Further investigation into the coherent detection scheme might reveal insights into this observed robustness against RIN variations.

Finally, we analyzed the impact of detection noise, specifically the dark current of the photodetectors. For our simulations, we set the responsivity to 0.9 $\frac{A}{W}$, consistent

with models such as the Thorlabs DX20 Series (20 GHz). We performed a sweep of dark current values ranging from 5 nA (typical low-noise detector performance) to 50 nA and 100 nA. Despite these variations, the SKR remained effectively unchanged, and the calibrated shot noise unit (SNU) baseline was identical across the cases. This suggests that the detection noise is dominated by the quantum noise generated by the photocurrent and that the NEP contributed by the dark current does not significantly degrade receiver performance under the tested conditions.

After evaluating the key noise contributions (modulation noise, laser linewidth and RIN, and detector dark current) we can conclude that, within our simulation framework, the system is primarily shot-noise-limited. Nonetheless, it is important to acknowledge that certain parameter configurations, particularly suboptimal modulation settings and broad laser linewidths, introduced substantial excess noise and severely limited protocol security. Therefore, while shot noise is the fundamental limiting factor under optimal settings, other noise sources become dominant under non-ideal conditions and must be carefully managed in practical implementations. In summary, these parameter sweeps and noise characterizations provided essential insights into the critical factors determining the practical performance and security of our CV-QKD protocol.

2.4.2 Protocol simulation and FSO scenario

Now that we have characterized our noise sources, we shift our focus to assessing the overall performance of our QKD protocol. A fundamental and practical question immediately arises when dealing with communication experiments: How far can we reliably transmit quantum-protected information?

Given our objectives, particularly considering potential future applications involving satellite-based communications, it is important to benchmark our results against relevant distances. However, to ground our study firmly within the context of established literature and to validate our simulations effectively, we begin by considering typical terrestrial fiber-optic distances frequently encountered in experimental quantum communication setups. Common benchmarks used in literature include 1 km, 4 km, 13 km, 20 km, and 40 km fiber spans.

Initially, during our detailed noise characterization phase, we utilized single-shot measurements, as this approach provided an efficient method for thoroughly exploring the extensive parameter space. Nevertheless, to authentically represent the statistical nature and practical variability inherent to quantum communications systems, it is essential to aggregate results from multiple measurement runs. Following the methodology established in [10] - [11], we executed each simulation scenario with eight measurement iterations.The SKR values quoted in Section 2.4.1 come from single-shot simulations at 13 km; averaged over eight runs, that distance no longer sustains a positive SKR.

Upon averaging the results across these multiple measurements, we obtained successful SKR for transmission distances of 1 km and 4 km, yielding respective SKRs of 2.54 Mbit/s and 0.39 Mbit/s. Unfortunately, beyond these distances (at 13 km, 20 km, and 40 km), the protocol failed to produce a positive secure key rate. The primary limiting factor observed at these longer distances was the increased impact

of the excess noise attributed to a potential eavesdropper. Despite the counterintuitive reduction of total excess noise at longer distances (due to increased losses in the optical link), the simultaneous drop in channel T and SNR significantly limited the achievable mutual information between Alice and Bob, making secure key generation impossible even under the relaxed (trusted-detector) security assumptions.

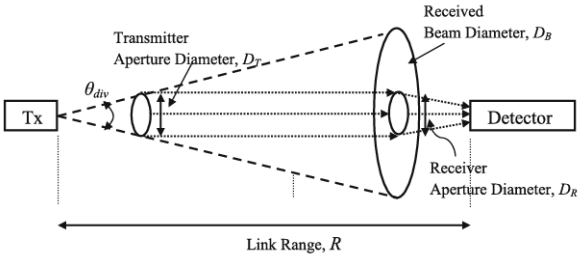


Fig. 8 Beam divergence in free space, adapted from [5].

To extend our analysis to the FSO scenario expected in an inter-satellite link, the optical-fiber channel is replaced by a variable optical attenuator. The attenuation values implemented in the protocol simulation are subsequently mapped onto an equivalent free-space range using an idealized diffraction-limited Gaussian-beam model. We consider a symmetric optical terminal with equal transmitter and receiver aperture diameters, as described in fig. 8, $D_{\mathrm{Tx}} = D_{\mathrm{Rx}} = 15$ cm, a value representative of the aperture scale considered for compact spaceborne optical terminals [33, 34]. The receiver radius is therefore $a_r = D_{\mathrm{Rx}}/2 = 7.5$ cm, corresponding to a collecting area $A_r = \pi a_r^2 \simeq 177$ cm^2. At the operating wavelength $\lambda = 1550$ nm, we assume an effective Gaussian beam waist $w_0 = 7.5$ cm. The corresponding diffraction-limited far-field half-angle divergence is $\theta_{\mathrm{div}} = \lambda/(\pi w_0) \simeq 6.6$ μrad.

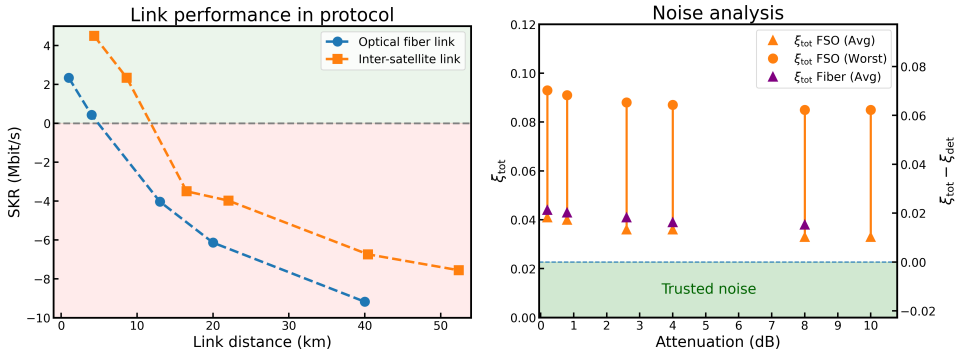


Fig. 9 (a) Comparison of the SKR obtained in the optical fiber experiment simulation and the free-space link. (b) Noise values obtained during the simulations. Left vertical axis represents total excess noise, while the right one represents the excess noise minus the detector noise calculated under the trusted detector assumption.

The fraction of the Gaussian optical power collected by a circular receiver aperture of radius a_r is $1 - \exp[-2a_r^2/w^2(R)]$. Since the variable attenuator in the protocol simulation represents the range-dependent channel loss, rather than the fixed aperture-coupling loss of the terminal, we normalize this quantity to its zero-range value. The equivalent geometric link attenuation is therefore

$$L_{\mathrm{geo}}(R) = -10\log_{10}\left[\frac{1-\exp\left(-2a_r^2/w^2(R)\right)}{1-\exp(-2a_r^2/w_0^2)}\right]. \tag{8}$$

This model provides an ideal geometric benchmark and does not include pointing and tracking errors, terminal optical inefficiencies, or additional implementation losses.

			FSO				**Optical Fiber**	
			averaged calib.		**worst-case calib.**		**averaged calib.**	
Att. [dB]	**T**	**SNR**	ξ_{tot}	$\xi_{\mathrm{tot}} - \xi_{\mathrm{det}}$	ξ_{tot}	$\xi_{\mathrm{tot}} - \xi_{\mathrm{det}}$	ξ_{tot}	$\xi_{\mathrm{tot}} - \xi_{\mathrm{det}}$
0.2	0.218	0.495	0.041	0.019	0.093	0.069	0.044	0.021
0.8	0.190	0.430	0.040	0.017	0.091	0.068	0.043	0.021
2.6	0.125	0.283	0.036	0.014	0.088	0.064	0.041	0.018
4.0	0.090	0.204	0.036	0.013	0.087	0.064	0.039	0.017
8.0	0.035	0.078	0.033	0.011	0.085	0.062	0.038	0.015
10.0	0.027	0.047	0.033	0.011	0.085	0.062		

Table 4 Parameter estimation for different attenuations, with excess noise values normalized to SNU. Comparison between averaged error values among the different simulation runs and the worst-case excess noise obtained among them.

As shown in figure 9(a) and table 4, the free-space link sustains a positive SKR up to a channel attenuation of 0.8 dB, corresponding to approximately 8.6 km, and aborts from 2.6 dB (≈16.5 km) onwards. Over these ranges the beam remains within its Rayleigh range ($z_R \approx 11.4$ km), so the geometric loss grows slowly with distance and the free-space link extends further than the fiber link. At equal channel attenuation, the free-space link also yields a higher SKR, consistent with the lower excess noise attributed to an eavesdropper in this scenario (table 4), which we attribute to the absence of dispersion in free space. Beyond the Rayleigh range, the loss grows quadratically with distance and, as in the fiber case, T and SNR rapidly fall to values that preclude a secure protocol.

We note that the transmittance T reported in table 4 includes, in addition to the channel attenuation, a fixed contribution of approximately 6.5 dB from the transmitter terminal. This accounts for the measured MZM insertion loss together with the excess loss of the MMI couplers and the fiber-to-chip coupling. Note that the 3.5 dB quoted for the MMI couplers in Section 2.4.1 corresponds to an isolated device and includes the intrinsic 3 dB splitting ratio, which is recovered upon recombination in the balanced modulator and therefore does not accumulate along the signal path. Because these terminal losses occur on Alice's side, before the untrusted channel, they are treated as trusted attenuation and are not attributed to an eavesdropper, placing the states entering the channel at the operating point quoted in Section 2.2.3.

To the best of our knowledge, this constitutes the first assessment of a CV-QKD architecture on a TFLN platform oriented towards inter-satellite links; no prior TFLN CV-QKD result, in fiber or free space, is available for direct comparison, and TFLN-based QKD demonstrations to date have been confined to the discrete-variable regime [19–21]. Since the integrated hardware is identical in both scenarios, the differences between the fiber and free-space results are governed by the channel itself, namely the distance dependence of the loss and the presence or absence of dispersion, rather than by the performance of the photonic chip, which behaves consistently across both channels.

At the same time, the free-space ranges reported here remain well below realistic inter-satellite distances, as the steep growth of attenuation with distance in figure 9 (a) makes explicit: extrapolating equation (8) with the same optical terminal to representative LEO inter-satellite separations of a few hundred kilometers yields link attenuations of approximately 15–25 dB for separations of 100–300 km, consistent with the loss budgets reported for LEO free-space quantum links [35]. Bridging this gap is a matter of link engineering rather than material platform: larger transmit/receive apertures, a reduced modulator half-wave voltage (Section 3), and advanced classical post-processing would all move the operating point towards operational inter-satellite budgets. A complete inter-satellite analysis would additionally need to account for pointing jitter and residual tracking errors, which our purely geometric Gaussian-beam model does not capture and which become significant loss and excess-noise contributions at these distances [35]. We therefore present these results as a hardware-anchored benchmark for CV-QKD on TFLN.

3 Conclusions

In this work, we presented a feasibility study of a CV-QKD transceiver architecture on a monolithic TFLN PIC oriented towards inter-satellite links, combining chip design and fabrication through a commercial MPW run, experimental characterization, radiation testing, and a hardware-anchored security simulation. To the best of our knowledge, this constitutes the first assessment of CV-QKD on the TFLN platform.

On the experimental side, we characterized passive and active building blocks across several chips from the MPW run, including bending, transmission, and crossing losses, extinction ratios, and half-wave voltages, with measured propagation losses (0.336 ± 0.127 dB/cm in 1 µm waveguides) competitive with foundry figures of merit and with other material platforms. These measurements validate the fabrication process and provide the realistic device parameters that anchor our simulations. Furthermore, the chips were exposed to gamma radiation in ascending doses up to 47 krad, after which passive, RF, and IQ modulation measurements showed no significant degradation. This validation of active TFLN PICs under radiation representative of space environments supports the suitability of the platform for satellite payloads; testing against other radiation sources present in space, such as protons and alpha particles, remains a relevant next step.

On the simulation side, our framework identified the critical noise sources of the protocol and optimized its operating parameters, showing that the system is primarily

shot-noise-limited under optimal settings. The resulting simulated secure key rates reach the Mbit/s range at short link distances, both in optical fiber (2.54 and 0.39 Mbit/s at 1 and 4 km) and in free-space links (up to approximately 8.6 km). The differences between both channel types are set by the channel loss and dispersion rather than by the integrated hardware. These distances remain well below operational inter-satellite requirements; as discussed in Section 2.4.2, bridging this gap is primarily a matter of link engineering and protocol refinement rather than of material platform.

Several simplifying assumptions delimit the scope of these results. The security analysis is asymptotic, treats detection noise as trusted, and applies the Gaussian framework to a QPSK constellation, as justified in Section 2.2.3; a discrete-modulation analysis incorporating finite-size effects would yield more conservative, implementation-faithful key rates and is a natural continuation of this work, together with advanced classical post-processing techniques [36, 37]. Likewise, certain device parameters, such as comprehensive waveguide losses and the frequency response of the EO phase shifters, are not yet fully characterized, and their inclusion will further improve simulation fidelity.

Finally, our noise characterization points to a clear design route for improvement: moderately extending the EO phase shifter length, within manageable centimeter-scale dimensions, would halve V_π, reducing modulation noise and the required laser power together with its associated noise contributions. Such focused design refinements, rather than platform or protocol changes, represent the most promising strategy to leverage the capabilities of TFLN and move integrated CV-QKD towards operational secure inter-satellite links.

In summary, this work contributes a fabricated and characterized TFLN PIC for CV-QKD, the first radiation validation of active TFLN photonics up to 47 krad, and a security analysis built on measured device parameters, yielding simulated key rates in the Mbit/s range. Together they establish TFLN as a viable platform for compact, radiation-tolerant quantum payloads and provide a reference point for the integrated CV-QKD systems that secure satellite constellations will require.

List of abbreviations

QKD	Quantum key distribution
CV-QKD	Continuous variable QKD
TFLN	Thin film lithium niobate
PIC	Photonic integrated circuit
RF	Radiofrequency
IQ	In-phase and Quadrature
FSO(C)	Free-space optical (communications)
SWaP	Size, weight and power
LEO	Low Earth Orbit
SKR	Secret Key Rate
SOI	Silicon on insulator
GMCS	Gaussian modulated coherent states

DM	Discrete modulated
InP	Indium phosphide
MPW	Multiproject wafer
EO	Electrooptic
DV-QKD	Discrete variable QKD
(L)LO	(Local) local oscillator
QPSK	Quadrature phase shift keying
SSB-CS	Single sideband with carrier suppression
FER	Frame error rate
SNR	Signal to noise ratio
SNU	Shot noise units
PIN	Positive intrinsic negative (diode)
MZM	Mach-Zehnder modulator
PDK	Project design kit
COTS	Commercial off the shelf
AWG	Arbitrary waveform generator
GSG	Ground signal ground (probes)
DC	Direct current
PCB	Printed circuit board
WG	Waveguides
PM	Polarization maintaining
MMI	Multimode interferometer
FOM	Figure of merit
RIN	Relative intensity noise
NEP	Noise equivalent power
ARC	Arquimea Research Center

Table 5: Abbreviations used in this document, by order of appearance

Declarations

Availability of data and materials

The datasets used and/or analysed during the current study are available from the corresponding author on reasonable request.

Competing Interests

The authors declare that they have no competing interests

Ethics Approval

Not Applicable

Funding

This work has been funded as part of the European project QCIRCLE (Teaming #SEP-210793656). This work has also been carried out within the frame of the project Cátedra PERTE Chip EPIQ (PERTE Chip #TSI-069100-2023-8).

Funded by the European Union. Views and opinions expressed are however those of the author(s) only and do not necessarily reflect those of the European Union. Neither the European Union nor the granting authority can be held responsible for them.

Authors' contributions

DMR performed the simulations and theoretical calculations for the prospective sections of this work. JCGC built the experimental setup and took the experimental measurements. JPR supervised communications measurements and hardware. CDF supervised and proofread this work.

Acknowledgements

Additional thanks to Borja Jerez for designing the PIC and leading the project at ARC, and Juan Lloret for the thermal control design of the experimental setup. Fabrication was carried out entirely by the foundry Luxtelligence. Special thanks to Alberto Beccari from Luxtelligence for the continous feedback and support on this behalf.

References

[1] Thylén L, Wosinski L. Integrated photonics in the 21st century. Photonics Research. 2014;2(2):75–81.

[2] Butt MA. Integrated optics: platforms and fabrication methods. Encyclopedia. 2023;3(3):824–838.

[3] Smit M, Williams K, Van Der Tol J. Past, present, and future of InP-based photonic integration. Apl Photonics. 2019;4(5).

[4] Lagunas E, Chatzinotas S, Ottersten B. Low-earth orbit satellite constellations for global communication network connectivity. Nature Reviews Electrical Engineering. 2024 Sep;1(10):656–665. https://doi.org/10.1038/s44287-024-00088-9.

[5] Kaushal H, Jain V, Kar S. Free space optical communication. vol. 60. Springer; 2017.

[6] Zhang G, Haw JY, Cai H, Xu F, Assad S, Fitzsimons JF, et al. An integrated silicon photonic chip platform for continuous-variable quantum key distribution. Nature Photonics. 2019;13(12):839–842.

[7] Zhu D, Shao L, Yu M, Cheng R, Desiatov B, Xin C, et al. Integrated photonics on thin-film lithium niobate. Advances in Optics and Photonics. 2021;13(2):242–352.

[8] Djordjevic IB. Physical-layer security and quantum key distribution. Springer; 2019.

[9] Ng SQ, Kanitschar F, Zhang G, Wang C. Gigabit-rate Quantum Key Distribution on Integrated Photonic Chips. arXiv preprint arXiv:250408298. 2025;.

[10] Laudenbach F, Pacher C, Fung CHF, Poppe A, Peev M, Schrenk B, et al. Continuous-variable quantum key distribution with Gaussian modulation—the theory of practical implementations. Advanced Quantum Technologies. 2018;1(1):1800011.

[11] Laudenbach F, Schrenk B, Pacher C, Hentschel M, Fung CHF, Karinou F, et al. Pilot-assisted intradyne reception for high-speed continuous-variable quantum key distribution with true local oscillator. Quantum. 2019;3:193.

[12] Lu CY, Cao Y, Peng CZ, Pan JW. Micius quantum experiments in space. Reviews of Modern Physics. 2022;94(3):035001.

[13] Li Y, Cai WQ, Ren JG, Wang CZ, Yang M, Zhang L, et al. Microsatellite-based real-time quantum key distribution. Nature. 2025;p. 1–8.

[14] Wang Z, Malaney R. Performance analysis of inter-satellite round-robin differential-phase-shift quantum key distribution. Quantum Information Processing. 2022 Sep;21(9). https://doi.org/10.1007/s11128-022-03673-9.

[15] Hajomer AAE, Bruynsteen C, Derkach I, Jain N, Bomhals A, Bastiaens S, et al. Continuous-variable quantum key distribution at 10 GBaud using an integrated photonic-electronic receiver. Optica. 2024;11(9):1197–1204.

[16] Hajomer AAE, Bomhals A, Bruynsteen C, Sidhique A, Kovalenko O, Derkach I, et al. Chip-based 16 GBaud continuous-variable quantum key distribution. Optica. 2026 Jun;13(6):1035–1042. https://doi.org/10.1364/OPTICA.590832.

[17] Aldama J, Sarmiento S, Vidarte LT, Etcheverry S, Grande IL, Castelvero L, et al. Integrated InP-based transmitter for continuous-variable quantum key distribution. Opt Express. 2025 Feb;33(4):8139–8149. https://doi.org/10.1364/OE.550386.

[18] Wang C, Zhang M, Chen X, Bertrand M, Shams-Ansari A, Chandrasekhar S, et al. Integrated lithium niobate electro-optic modulators operating at CMOS-compatible voltages. Nature. 2018;562(7725):101–104.

[19] Lin Z, Gao Y, Zhou L, Yuan H, Zhu Y, Lin Z, et al. Integrated lithium niobate photonics for high-speed quantum key distribution. Optica Quantum. 2025;3(2):195–200.

[20] Heo H, Woo MK, Park CH, Jang HS, Hwang H, Lee H, et al. On-chip quantum key distribution over field-deployed fiber using lithium niobate photonic circuit. APL Photonics. 2025;10(3):031301.

[21] Bernardi A, Clementi M, Bacchi M, Bolaños MR, Congia S, Garrisi F, et al. Gigahertz-rate thin-film lithium niobate receiver for time-bin quantum communication. Light: Science & Applications. 2026;15:237.

[22] Jiang P, Balram KC. Suspended gallium arsenide platform for building large scale photonic integrated circuits: passive devices. Optics express. 2020;28(8):12262–12271.

[23] Huang JZ, Weedbrook C, Yin ZQ, Wang S, Li HW, Chen W, et al. Quantum hacking of a continuous-variable quantum-key-distribution system using a wavelength attack. Physical Review A—Atomic, Molecular, and Optical Physics. 2013;87(6):062329.

[24] Ma XC, Sun SH, Jiang MS, Liang LM. Wavelength attack on practical continuous-variable quantum-key-distribution system with a heterodyne protocol. Physical Review A—Atomic, Molecular, and Optical Physics. 2013;87(5):052309.

[25] Leverrier A, Grangier P. Unconditional security proof of long-distance continuous-variable quantum key distribution with discrete modulation. Physical Review Letters. 2009;102(18):180504.

[26] Ghorai S, Grangier P, Diamanti E, Leverrier A. Asymptotic security of continuous-variable quantum key distribution with a discrete modulation. Physical Review X. 2019;9(2):021059.

[27] Lin J, Upadhyaya T, Lütkenhaus N. Asymptotic security analysis of discrete-modulated continuous-variable quantum key distribution. Physical Review X. 2019;9(4):041064.

[28] Denys A, Brown P, Leverrier A. Explicit asymptotic secret key rate of continuous-variable quantum key distribution with an arbitrary modulation. Quantum. 2021;5:540.

[29] Kanitschar F, Pacher C. Optimizing continuous-variable quantum key distribution with phase-shift keying modulation and postselection. Physical Review Applied. 2022;18(3):034073.

[30] Nazca.: Homepage. Last accessed Oct 2024. Available from: https://nazca-design.org/.

[31] Luxtelligence.: Foundry homepage. Last accessed May 2026. Available from: https://luxtelligence.ai/.

[32] Akah H, Elfiky D, Shahin K, Elemam E, Anwar A. Total Ionizing Dose Effects on Commercial ARM Microcontroller for Low Earth Orbit Satellite Subsystems. International Conference on Aerospace Sciences and Aviation Technology. 2017 April;17. https://doi.org/10.21608/asat.2017.22762.

[33] Khanna A, Majumder S, Jain A, Singh DK. Quantum BER estimation modelling and analysis for satellite-based quantum key distribution scenarios. IET Quantum Communication. 2024;5(2):157–163. https://doi.org/https://doi.org/10.1049/qtc2.12081. https://ietresearch.onlinelibrary.wiley.com/doi/pdf/10.1049/qtc2.12081.

[34] Smutny B, Kaempfner H, Muehlnikel G, Sterr U, Wandernoth B, Heine F, et al. 5.6 Gbps optical intersatellite communication link. Proc SPIE. 2009 02;7199:719906. https://doi.org/10.1117/12.812209.

[35] Dequal D, Trigo Vidarte L, Roman Rodriguez V, Vallone G, Villoresi P, Leverrier A, et al. Feasibility of satellite-to-ground continuous-variable quantum key distribution. npj Quantum Information. 2021;7:3.

[36] Dong C, Cheng J, Liu A, Chen L, Chen Y, Yin P, et al. Machine learning for optimal parameter prediction in free space continuous-variable quantum key distribution. New Journal of Physics. 2025;.

[37] Li D, Huang P, Zhou Y, Li Y, Zeng G. Memory-saving implementation of high-speed privacy amplification algorithm for CV-QKD. IEEE Photonics. 2018;10(5):1–12.